ACS APPLIED ENGINEERING MATERIALS

pubs.acs.org/acsaenm Article

Nickel-Coated Aluminum Nanoparticles for Modulating Ignition Temperature: Interfacial Chemistry and Mechanism

Yuxin Zhou,[†] Lei Yang,[†] Ashvin Kumar Vasudevan, Matthew Dickson, Mahbub Chowdhury, Keren Shi, and Michael R. Zachariah*

Cite This: *ACS Appl. Eng. Mater.* 2025, 3, 2346−2353

Read Online

ACCESS | Metrics & More | Article Recommendations | Supporting Information

Downloaded via UNIV OF CALIFORNIA RIVERSIDE on January 11, 2026 at 23:34:15 (UTC).
See https://pubs.acs.org/sharingguidelines for options on how to legitimately share published articles.

ABSTRACT: Metal particles such as Al always have a native oxide shell, which acts as a barrier to unintended ignition but can also significantly retard the combustion chemistry. Herein, we present a strategy to trigger ignition using Al−Ni intermetallic reactions. The approach involves synthesizing Ni-coated Al (Al@Ni) nanoparticles, whose ignition temperature can be significantly reduced (up to ~230 K), and the reduction can be tuned by adjusting the amount of Ni deposited via a kinetic control strategy. The underlying ignition enhancement mechanism of Al@Ni is explored through differential scanning calorimetry, environmental transmission electron microscopy, and reactive molecular dynamics simulations. Two major factors contribute to the reduced ignition temperature: (1) the highly exothermic Al−Ni intermetallic reaction that occurs before ignition, driven by the diffusion or bulk flow of Al from the Al core through the oxide shell to Ni, and (2) the retardation of Al nanoparticle sintering, which is beneficial to both ignition and consequent oxidation reactions. Owing to the decreased ignition temperature, Al@Ni-based propellant demonstrates an ~26% higher regression rate compared to native Al.

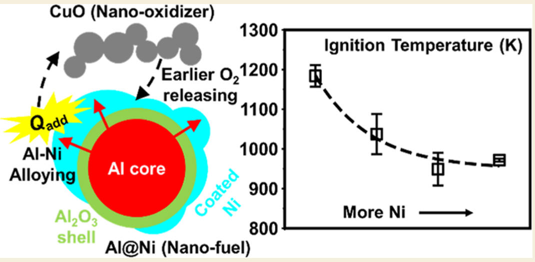

KEYWORDS: *aluminum nanoparticles, nickel coating, energetic materials, intermetallic reactions, ignition, molecular dynamics*

1. INTRODUCTION

Aluminum (Al) is extensively utilized as an additive in propellants, explosives, and pyrotechnics due to its superior energy density, compared to conventional hydrocarbon fuels.[1] Various factors can influence the ignition temperature of Al particles, with particle size being one of the most critical and widely studied. The ignition temperature of Al can drop significantly from ~2350 K (the melting point of its oxide shell) to as low as ~1000 K when the particle size decreases from microscale to nanoscale, which is generally attributed to the cracking of the oxide shell induced by the tensile stress from the molten Al core.[2] Another key factor affecting ignition behavior is the thickness of the oxide shell, since Al particles are typically covered by a layer of native alumina (Al_2O_3). Thicker oxide shells have been shown to delay the ignition significantly during fast-heating experiments,[3] supporting a diffusion-controlled ignition mechanism. Additionally, the processes of sintering and coalescence, which can lead to the loss of nanostructures during combustion, are other critical factors that inhibit the rapid and complete energy release of aluminum nanoparticles, affecting their overall reactivity.[4−8]

Inorganic or organic coating has been demonstrated as an effective way to enhance the performance of Al microparticles.[9] Recent studies[10,11] showed improved combustion properties of Al when functionalized with ammonium perchlorate (AP) or fluorocarbon species through methods such as heterogeneous nucleation or silylation chemistry. Additionally, Al particles coated with transition metals via electroless plating techniques have opened up new possibilities,[12−14] initially driven by efforts to inhibit Al passivation.[15] Ali et al.[12] synthesized Fe-coated Al microparticles by replacement and found that Fe-coated Al exhibited a 2.7× energy release intensity compared to the uncoated. Xiao et al.[16] prepared copper pentafluorobenzoate-coated Al microparticles and reported that the ignition delay time was reduced. Hahma et al.[17] observed that both nickel coating and cobalt coating could prevent particle agglomeration during the combustion. Wang et al.[13] observed improved ignition and combustion performance of micron-sized Al particles coated with a nickel−phosphorus alloy. Among these transition metals, nickel-coated aluminum (Al@Ni) stands out for its ability to significantly lower the ignition temperature for micron-sized Al particles. Zhang et al.[14] also reported a ~10% improvement in the regression rate of propellants after applying micron-sized Al@Ni additives.

While Al@Ni has garnered significant research interests,[14,18,19] a fundamental understanding of its improved ignition properties remains unclear. Several theories have

Received: April 13, 2025
Revised: July 23, 2025
Accepted: July 24, 2025
Published: July 29, 2025

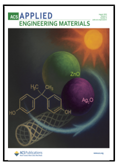

ACS Publications © 2025 American Chemical Society

https://doi.org/10.1021/acsaenm.5c00272

been proposed to explain the exceptional combustion performance of Al@Ni, including intermetallic reactions initiated by molten aluminum infiltrating the Ni shell,[19] diffusion of aluminum or oxygen, and oxidation processes occurring at grain boundaries.[20,21] However, the precise mechanism governing the combustion of nanoscale Al@Ni remains controversial; the existing studies are predominantly conducted with micron-sized particles[14,18−21] because the synthesis of nanoscale Al@Ni remains challenging. For instance, Zhang et al.[14] and Li et al.[18] employed NH_4F or NaOH to eliminate the oxide shell respectively, followed by a replacement reaction between micron Al and $NiCl_2$ to deposit Ni on the bare Al particle surfaces. However, applying this approach to nanoscale particles poses significant challenges, as bare nanosized Al particles are highly susceptible to rapid oxidations in solutions.

In this work, a one-pot, scalable, and cost-effective method to fabricate Al@Ni nanoparticles is utilized to manipulate the ignition behavior of Al nanoparticles by controlling the condensation of Ni. The synthesized Al@Ni nanoparticles are comprehensively investigated by differential scanning calorimetry (DSC), in situ transmission electron microscopy (TEM), and reactive molecular dynamics (MD) simulations, with an overall reaction mechanism proposed. Direct observation of the diffusion and molten leaking processes of Al into Ni by in situ TEM validates their interaction mechanism and confirms the existence of the intermetallic reactions.

2. METHODS

2.1. Materials

To synthesize Al@Ni nanoparticles, ammonia borane (NH_3BH_3, Sigma-Aldrich, 90%), and nickel(II) chloride hexahydrate ($NiCl_2 \cdot 6H_2O$, Alfa Aesar, 99.95%) are used as the reducing agent and nickel source, respectively. Each precursor is dissolved separately in analytical-grade methanol (Fisher Scientific, 99.9%). Then the nickel solution is mixed with Al nanoparticles (US Research Nanomaterials, nominal diameter: 100 nm). Subsequently, NH_3BH_3 solution is introduced to initiate the coating reaction, as shown by eq 1.[22−24] The treatment is accompanied by ultrasonication at ∼313 K to ensure complete dispersion and uniform mixing; and the treatment times are varied from 40 to 120 min to adjust the amount of condensed Ni. Upon completion of the reaction, the nanoparticles are harvested by centrifugation at 10,000 rpm for 10 min, halting shell growth, and minimizing potential residual nickel salts and byproducts. Subsequently, additional analytical-grade methanol is used to wash the product for the further removal of any remaining impurities. The resulting Al@Ni is then dried at room temperature for at least 24 h. The diagram of this one-pot synthesis method is shown in Figure 1a. A detailed formulation list, including the weight of each reagent, is provided in Table S1. The yield of each synthesis batch is typically ∼100 mg. However, a 10× scale-up experiment is also performed to demonstrate its potential for scalability using the same recipe.

$$2NiCl_2 + NH_3BH_3 = 2Ni + NH_4BCl_4 + H_2 \tag{1}$$

Scanning electron microscopy (SEM) images of Al@Ni in Figure 1b show that although the nominal average of commercial Al nanoparticles is 100 nm, a few particles with microscale dimensions (but less than 5 μm) are present. After synthesis, the average particle size slightly increases because of Ni coating and the loss of smaller particles during centrifugation, as illustrated by particle size distribution results in Figure S1. Nevertheless, the synthesized Al@Ni largely retain their original distribution, indicating that the coating process has minimal impact on the overall particle size. Figure 1c,d shows representative scanning transmission electron microscopy (STEM) images and energy-dispersive X-ray spectroscopy (EDS) maps of nanosized Al@Ni, and more STEM/EDS results can be found in our later discussion and Supporting Information. These images confirm that most Al nanoparticles are uniformly coated with a nickel layer measuring several nanometers in thickness. Although ultrasonication is performed to mitigate particle agglomeration, inhomogeneity in the Ni coating exists, as highlighted by the bulk Ni in Figure 1c,d.

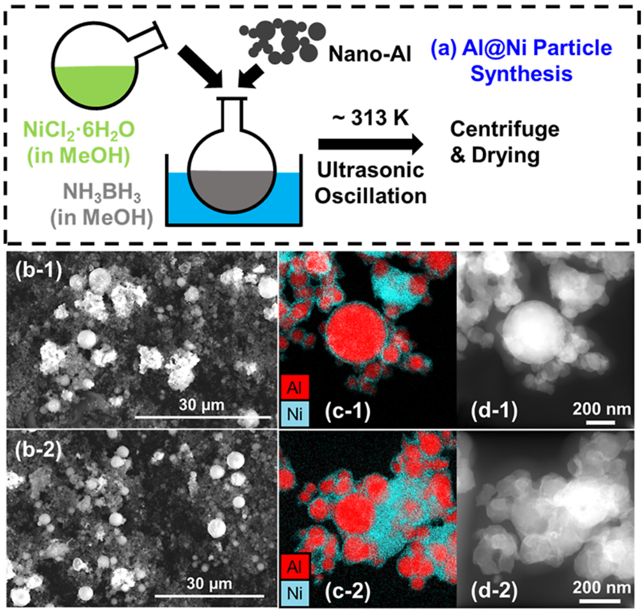

Figure 1. (a) One-pot synthesis methodology of Al@Ni nanoparticles; (b) SEM images, (c) EDS maps, and (d) STEM images of Al@Ni nanoparticles.

For a better comparison to Al@Ni, physically mixed Al nanoparticles and Ni nanoparticles (PM Al−Ni), Al_2O_3@Ni, and Al nanoparticles without any condensed Ni are also prepared. PM Al−Ni are prepared by mixing Al nanoparticles and Ni nanoparticles (Sigma-Aldrich, nominal diameter: <100 nm) with the Al/Ni molar ratios of 4:1 and 8:1, respectively, in hexane under ultrasonication for >30 min. For the synthesis of Al_2O_3@Ni, the procedures are the same as Al@Ni except for the use of Al_2O_3 nanoparticles (Sigma-Aldrich, nominal diameter: <50 nm). The Al nanoparticles used for comparison are soaked in the methanolic solution of $NiCl_2$ (without any NH_3BH_3 addition) and then separated using the same procedure as Al@Ni, to eliminate the potential influences of methanol, residual salts, and bound water.

2.2. Temperature-Jump Ignition and Time-of-Flight Mass Spectrometry

Temperature-jump (T-jump) ignition and T-jump time-of-flight mass spectrometry (TOFMS) are used for the measurement of ignition temperature and the identification of gas-phase species released from ignition, respectively. A more detailed description of T-jump ignition and T-jump TOFMS can be found in our previous work.[25,26] Fuel (Al@Ni or Al) and oxidizer (CuO) nanoparticles are physically mixed and then deposited on a Pt wire (diameter ∼76 μm, length ∼1.0 cm). The equivalence ratio is ∼0.67 (fuel-lean) to pursue a more complete oxidation. A 3 ms high-voltage pulse is applied to the Pt wire to induce rapid heating (∼10^5 K/s). The temperature of the Pt wire is then calculated from the electrical resistance by measuring the voltage and current during heating.

For measurement of the ignition temperature, a high-speed monochromic camera (Vision Research Phantom V12.1) operated at 67,000 fps is employed to measure the ignition delay time of the fuel and oxidizer nanoparticles deposited on the Pt wire in an argon atmosphere. Then the recorded delay time is correlated with the temperature of the Pt wire to determine the ignition temperature.

For TOFMS, fuel and oxidizer nanoparticles are ignited in an ultrahigh vacuum environment (<1.8 × 10^{-7} Torr), and the gas-phase species released are ionized by 70 eV electron beams. Ionized species are then accelerated in a linear time-of-flight chamber with their time-resolved mass spectra captured by a microchannel plate detector and recorded with a digital oscilloscope (Teledyne Lecroy). The temperature of the Pt wire was also measured simultaneously.

2.3. Preparation of Aluminized Propellants

60 mg of modified methylene diphenyl isocyanate curative and 52 mg of isodecyl pelargonate (IDP) plasticizer are mixed with 408 mg of HTPB resin for 5 min at 2000 rpm using a Thinky AR100 planetary mixer. Subsequently, 650 mg of ground ammonium perchlorate (AP, Alfa Aesar, >95%) is added as the oxidizer and mixed for an additional 10 min to achieve a homogeneous distribution. Afterward, 130 mg of Al nanoparticles or Al@Ni nanoparticles is incorporated into the formulation and mixed for another 10 min. During the casting process, the resulting mixture is pressed with a syringe to remove entrapped air, ensuring uniformity and density in the final material. The propellant-filled syringe is left undisturbed for >1 day at room temperature to allow for complete curing of the HTPB. Once cured, the solid propellant grain is sectioned into ∼1 cm for combustion. HTPB/AP propellants without any particles are also prepared.

2.4. Regression Rate Measurement of Aluminized Propellants

The regression rate of propellants is calculated by dividing the length of the propellant by the total burning time, as measured using a high-speed camera (Vision Research Phantom Miro M110) operating at 200 fps. Prior to the experiments, the propellant is positioned upright on a plate, with a coiled NiCr ignition wire placed at its top. The side of the propellant is covered with graphene powder to help with linear regression. Subsequently, the ignition coil is heated with direct current, simultaneously triggering the camera to capture the combustion process in real time.

2.5. Thermogravimetric Analysis and DSC

Thermogravimetric analysis (TGA) and DSC of the samples mentioned above are performed in a NETZSCH STA 449 F3 Jupiter thermogravimetric analyzer. All samples are heated to 1473 K in alumina crucibles with a ramp rate of 10 K/min under an ultrapure Argon flow (50 mL/min) to characterize exothermic or endothermic reactions. Roughly 2−3 mg of sample is used for each TGA/DSC run.

2.6. SEM, TEM, and In Situ TEM

Al@Ni in Figure 1b is observed by an FEI Nova NanoSEM 450. In situ observation of the structural dynamics of the Al@Ni and Al_2O_3@Ni nanoparticles at controlled heating temperature and EDS analysis on the element compositions is accomplished with a STEM (FEI Titan Themis 300). An X-FEG electron gun used with high-voltage ranging from 200 to 300 kV allowed for high-resolution TEM or STEM imaging. Note that the temperature of the vacuum cell is measured by probing the resistance of the SiC base film, while monitoring the specific temperature of each particle is challenging due to ongoing reactions.

2.7. Reactive MD Simulation

Besides the aforementioned experiments, MD simulation is also performed in LAMMPS,[27] with ReaxFF developed by van Duin and his co-workers,[28−30] to study the interfacial chemistry in Al@Ni at the atomic level. To efficiently simulate the diffusion of Al atoms at the interface between the Al nanoparticle and its Ni shell, three thin layers of Al, Al_2O_3, and Ni are used in the simulation domain of 40 Å (length) × 40 Å (width) × 80 Å (height). Initially, the Al layer, Al_2O_3 layer, and Ni layer (5211 atoms in total) are taken from the ideal lattices; then, they are combined, relaxed (energy minimization), and heated at 400 K to reach a relatively stable state. Then the temperature was elevated to 800 K to observe the diffusion of Al. To approximate the infinite extent of bulk Al, the Al atoms at the bottom of the simulation domain (361 atoms) are frozen to create a fixed boundary. The total simulation time is 140 ps, including 5 ps for heating the ideal lattice to 400 K, 25 ps for stabilizing the entire system at 400 K, 5 ps for further heating to 800 K, and 105 ps for stabilizing the entire system at 800 K. NVT ensemble with Nose−Hoover thermostat[31] is employed and the time-step for all stages in this simulation is 0.2 fs. The number of Al−Ni bonds is calculated based on a bond-order cutoff value of 0.3.

3. RESULTS AND DISCUSSION

3.1. Al@Ni in Nanothermite: T-Jump Ignition and TOFMS

Figure 2a shows the ignition temperatures of Al@Ni nanoparticles physically mixed with CuO as nanooxidizers (equivalence ratio $\varphi \approx 0.67$) during T-jump experiments conducted on an ultrafine Pt wire in the argon atmosphere. The temperature of the Pt wire can ramp from room temperature to roughly 1300 K within 3 ms. As presented in the snapshots of the ignition process in Figure 2a,b, Al@Ni/CuO ignites within 2 ms, with the Pt wire still appearing dark; conversely, Al/CuO gets ignited after 2 ms, at which point the Pt wire has become noticeably bright. Al@Ni shows a shorter ignition delay time compared to Al, when temperature ramp rates similar. More details about ignition delay times are presented in Table S2. By correlating the ignition time observed by high-speed imaging with the temperature evolution of the Pt wire, the average ignition temperature of Al@Ni/CuO (treatment time = 80 min) is calculated to be ∼950 ± 40 K from three individual runs, significantly lower than that of Al/CuO by approximately 230 K. Despite the lower specific energy of Ni compared to Al, Al@Ni shows an improved ignition performance in nanothermite applications.

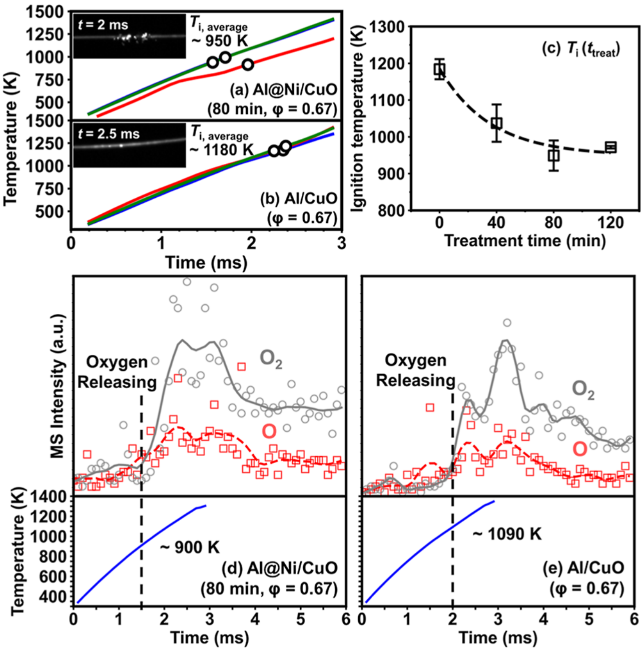

Figure 2. Ignition temperature: (a) Al@Ni/CuO and (b) Al/CuO during their T-jump in argon. Red, blue, and green curves in subfigures (a) and (b) represent the temperature profiles of the Pt wire during three individual runs, and the three hollow symbols represent respective ignition temperatures. Snapshots of ignition are attached in subfigures (a) and (b). (c) Ignition temperatures of Al@Ni/CuO with different treatment times of Al@Ni. Mass spectrometry: MS signal of O/O_2 (upper panel) and the corresponding temperature profile of the Pt wire (lower panel) during the T-jump of (d) Al@Ni/CuO and (e) Al/CuO in argon.

By adjustment of the treatment duration of Al nanoparticles in the coating solution, one can control the amount of Ni deposited on the Al core. As illustrated in Figure 2c, a treatment time of zero represents uncoated Al nanoparticles, which exhibit an ignition temperature of ∼1180 ± 30 K when mixed with nanosized CuO to form a thermite mixture. Increasing the treatment time to 40 and 80 min lowers the ignition temperatures to ∼1050 ± 50 K and ∼950 ± 40 K, respectively. Lee et al.[32] reported a similar phenomenon for Ni-coated Al microparticles (i.e., ignition delay time in shock tube decreases as the weight percentage of Ni increases), further demonstrating the enhancement effect of Ni. However, extending the treatment time to 120 min did not lead to a further decrease in ignition temperature. The plateau stage in ignition temperature may be caused by two reasons, i.e., (1) the deposition of nickel from solution reaches saturation on the available Al surface, thus achieving a kinetic equilibrium; or (2) the drawbacks of the nickel coating such as its relative low energy density and acting as diffusion barrier of O_2 gradually dominates as the Ni layer thickness increases. This demonstrates that kinetic control is an easy way to modulate the ignition temperature of Al@Ni. Meanwhile, the 10× scale-up experimental result on Al@Ni (treatment time = 80 min) shows no significant difference in ignition temperature.

Gas-phase species released during the ignition of Al@Ni/CuO (treatment time = 80 min) and Al/CuO are analyzed using T-jump TOFMS. Temporal monitoring of the O/O_2 during the ignition of Al@Ni/CuO shows a rapid increase at 0.5 ms, earlier than that of the Al/CuO, consistent with the observed lower ignition temperature for the Al@Ni/CuO. The release of oxygen occurs before ignition by roughly 0.2 ms, as compared to T-jump ignition and T-jump TOFMS. Since the CuO used in the two thermites is identical, the earlier release of oxygen can only be attributed to the difference in local temperature. Here, we suggest that additional heat released from Al@Ni contributes to the earlier oxygen release of CuO, and it will be confirmed in DSC experiments in Section 2.3.

3.2. Al@Ni in Propellant: High-Speed Imaging

The T-jump experiments discussed in Section 2.1 demonstrate the lowering of the ignition temperature with Al@Ni. In this section, we further explore its behavior in a hydroxyl-terminated poly(butadiene)/ammonium perchlorate (HTPB/AP) propellant. High-speed imaging is employed to investigate the burning behavior of free-standing HTPB/AP propellant, HTPB/AP/Al, and HTPB/AP/Al@Ni propellant in air at room temperature and atmospheric pressure, as shown in Figure 3a. The average propellant regression rate of HTPB/AP/Al@Ni propellant calculated from three individual runs is 0.97 ± 0.12 mm/s, ∼26% higher than that of the HTPB/AP/Al propellant (0.77 ± 0.08 mm/s) and ∼80% higher than that of the HTPB/AP propellent (0.54 ± 0.03 mm/s), as shown in Figure 3b. The HTPB/AP/Al propellant regresses faster than HTPB/AP since Al nanoparticles are more reactive than HTPB, while Al@Ni can further promote regression since the lower ignition temperature of Al@Ni possibly allows ignition earlier, thereby facilitating greater heat feedback to the unburned zone.

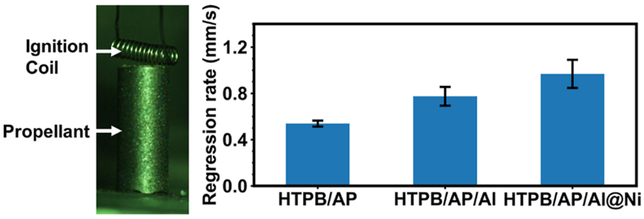

Figure 3. Propellant (HTPB/AP, HTPB/AP/Al, and HTPB/AP/Al@Ni) regression rate measurement setup (left) and results (right).

Meanwhile, some previous studies have indicated that Ni and NiO exhibit catalytic effects on AP decomposition and HTPB pyrolysis, respectively,[33−35] which possibly represents another potential advantage offered by Al@Ni nanoparticles.

Again, it is important to note that nickel itself is not a highly energetic material. As a result, nickel coating may lead to a reduction in the overall heat of combustion. However, this impact on the performance of propellant is limited since the mass fraction of nickel in the propellant is relatively low (<5%) and the trade-off is justified by the significant improvement of propellant regression.

3.3. Mechanism Study

Figure 4 presents the baseline-subtracted DSC profiles of Al@Ni nanoparticles with different treatment times. For a better comparison, physically mixed Al and Ni nanoparticles in a molar ratio of 4:1 (PM Al−Ni), nickel-coated alumina nanoparticles (Al_2O_3@Ni), and Al nanoparticles are also examined. DSC experiments are performed in a thermogravimetric analyzer in argon. TGA profiles demonstrate that the mass change is negligible, assuring that oxidation can be ruled out here. All of the DSC profiles in Figure 4 are baseline-subtracted. No remarkable thermal behaviors can be found below 600 K. Raw TGA/DSC data can be found in Figures S2 and S8 in the Supporting Information.

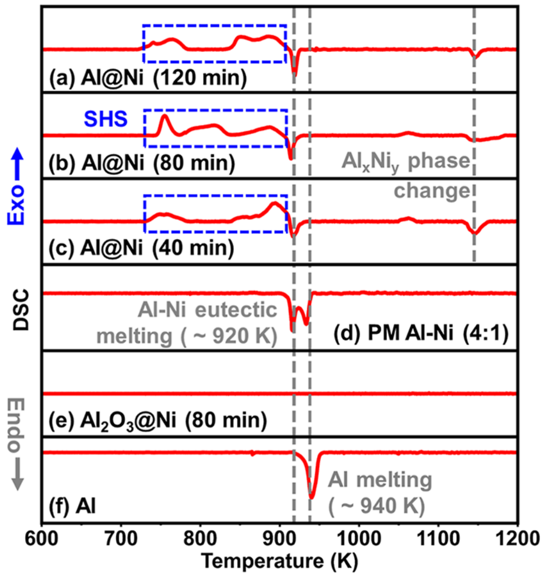

Figure 4. DSC profiles of (a) Al@Ni (treatment time = 120 min), (b) Al@Ni (treatment time = 80 min), (c) Al@Ni (treatment time = 40 min), (d) PM Al−Ni (molar ratio 4:1), (e) Al_2O_3@Ni (treatment time = 80 min), and (f) Al nanoparticles.

Al nanoparticles show a single endothermic peak at ∼940 K, corresponding to their melting point. For PM Al−Ni (4:1), in addition to the endothermic melting of pure Al at ∼940 K, another endothermic peak appears at ∼920 K, which can be attributed to the eutectic melting of Al (s) + Al_3Ni (s) according to the phase diagram and previous studies.[36−39] PM Al−Ni (8:1) shows qualitatively consistent results with PM Al−Ni (4:1). In contrast, Al_2O_3@Ni shows no evidence of endothermic or exothermic reactions, as both Al_2O_3 and Ni cannot melt within this temperature range, nor should they react based on thermodynamic considerations. This also demonstrates that Ni would not interact with the Al_2O_3 shell during the synthesis process.

For Al@Ni nanoparticles, the most noteworthy finding is the emergence of a series of exothermic peaks at a relatively low-temperature range (starting at ~750 K and continuing until the eutectic melting point). Unlike the melting events that occur in a narrow temperature range, these exothermic events span a wide temperature range, which is very likely caused by the inhomogeneity of Ni coating. These exothermic events are believed to represent the alloying reactions between Al and Ni, leading to the formation of Al−Ni alloys (likely 3Al (s) + Ni (s) = Al_3Ni (s), $\Delta H^\circ = -164$ kJ/mol); the alloying reactions can be further confirmed by the X-ray diffraction (XRD) analysis on the postproduct, which reveals a pronounced presence of Al_3Ni as well as a minor amount of Al_3Ni_2, as illustrated by Figure S10. Notably, the area of alloying exothermic peaks of Al@Ni with a 40 min treatment is smaller than those for 80 and 120 min samples, suggesting a smaller Ni content in the 40 min sample. Eutectic melting can also be observed in all Al@Ni samples, regardless of the treatment times. Exothermic alloying reactions may continue during the melting process, with the heat generated partially compensating for the heat absorption of melting, resulting in a smaller endothermic peak. Meanwhile, Al@Ni samples do not exhibit the characteristic pure Al melting endothermic peak at ~940 K, which implies that there is almost no pure Al in the Al@Ni sample. In short, Al partially reacts with Ni to form Al_3Ni alloy at 750−910 K, and the resultant Al (s) + Al_3Ni (s) melts at ~920 K to form Al (l) + Al_3Ni (s). The endothermic peak observed at ~1140 K is associated with the phase change of the generated Al−Ni alloy, most probably the melting of Al_3Ni or the phase transformation from Al_3Ni to Al_3Ni_2 according to phase diagram.[39,40] Compared to PM Al−Ni, which exhibits limited Al_3Ni formation and insufficient heat release due to poor Al−Ni interactions, Al@Ni demonstrates significantly exothermic alloying and greater Al_3Ni alloy formation. An elucidative phase diagram and detailed peak assignments of the thermochemical steps involved in the heating process of Al@Ni, PM Al−Ni, and Al are provided in Figure S9 and Table S3 in the Supporting Information.

The additional heat, generated from the exotherms that appear in the low-temperature range, is likely a major factor enhancing the ignition properties of Al@Ni/CuO nanothermites observed in T-jump experiments.

Next, we map the DSC exotherm with physical changes to the particle structure with in situ environmental TEM. Al@Ni with a treatment time of 80 min is chosen for these experiments. Both the final product of Al@Ni in TG/DSC analysis and Al@Ni directly heated in in situ TEM are examined.

While it is expected that Al reacts with the surrounding Ni when melting-induced density changes cause oxide shell cracking and Al outflow, the DSC results indicate that these reactions can occur at temperatures much lower than the melting point of Al. TEM observations confirm that Al−Ni alloying can begin before Al melts, driven by the diffusion of Al through its oxide shell. Figure 5a shows the structure of Al@Ni after being heated to 793 K (right after the first exothermic peak) in TG. When Al@Ni is heated, the thin Ni layer around the Al nanoparticles exhibits a tendency to sinter, forming small "crowns".[41] The nonoverlapping O EDS signal and Ni EDS signal indicate that Ni is located outside the oxide shell, suggesting that the presence of nickel oxide is unlikely. Ni sintering to "crowns" is also observed in Al_2O_3@Ni, detailed in supplementary Figures S11−S14. However, Ni sintering can hardly lead to any observable exotherms, as demonstrated by the flat DSC of Al_2O_3@Ni. Rather, Al diffuses into these Ni "crowns", as highlighted by the dashed boxes in Figure 5a. The Al particle at the top-right corner (in green dashed boxes in Figure 5a), which has more nickel coating, shows more complete outward diffusion of Al, resulting in a sparser Al signal inside the particle.

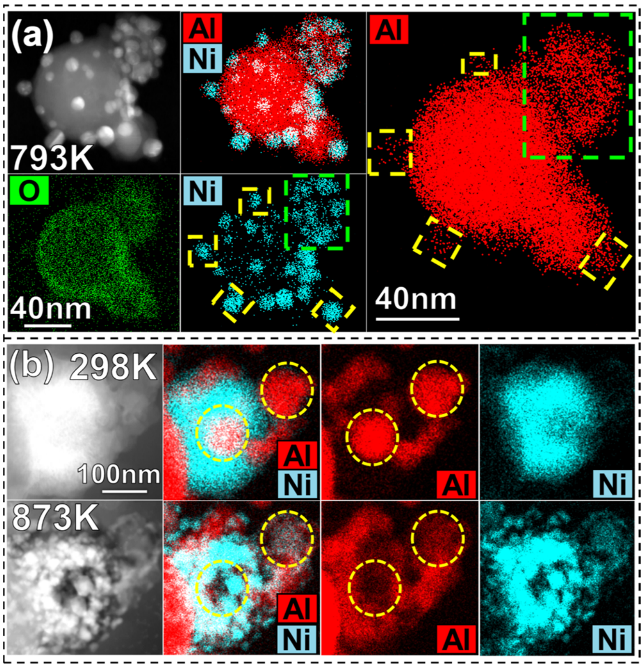

Figure 5. (a) STEM images and EDS maps of the product obtained after heating Al@Ni to 793 K in TGA; (b) in situ STEM images and EDS maps of Al@Ni in a vacuum cell at 298 and 873 K, respectively.

This diffusion pattern of Al is further corroborated by Figure 5b, which shows an Al@Ni nanoaggregate with a very thick Ni layer (or "bulk Ni") heated directly from 298 to 873 K in a vacuum cell of in situ TEM. At 873 K, the Al cores (highlighted by the yellow circles) nearly disappear, while their surroundings show increased Al EDS signal compared to 298 K. This observation suggests outward diffusion of Al into Ni layers, which is not observed in thin Ni layer scenarios. Additionally, the outwardly diffused Al can react with Ni, generating heat that may facilitate the melting of the Al core, followed by the cracking of alumina shells and the subsequent outflow of molten Al. The latter point is consistent with our observation of the melting of the Al core at an ~873 K environmental temperature (Figure S15).

Another observed advantage of Al@Ni nanoparticles is the ability of the Ni shells to inhibit the sintering of Al nanoparticles. As illustrated in Figure 6, an Al@Ni nanoaggregate is heated from 298 to 873 K in the in situ TEM. Al particles with conformal Ni coatings (left side in yellow box) retain their nanostructure after being heated to 873 K. In contrast, Al nanoparticles with nonconformal Ni coatings (right side in green box) sintered into larger particles. This comparison underscores the role of Ni coating in preserving nanostructure, which is a primary concern in the use of

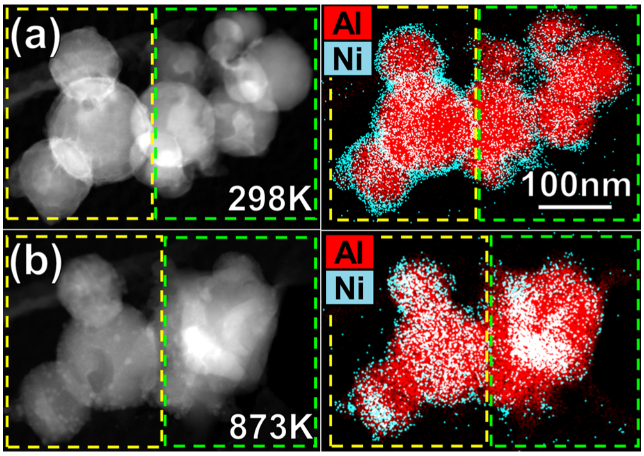

Figure 6. STEM images and EDS maps of Al@Ni in a vacuum cell at 298 K (a) and 873 K (b).

nanostructured fuels.[6,7] More detailed EDS maps regarding Figure 6, including the oxygen signal, are presented in Figure S16.

To better understand the interface reaction, MD simulations are used to provide atomic insight. Figure 7a−c shows a stacked layering of Al, Al_2O_3, and Ni to simulate the interface of Al@Ni nanoparticles, initially thermally stabilized at 400 K, followed by a temperature increase to 800 K. Upon heating to 800 K, both the oxide shell and the nickel shell appear to maintain their structural integrity and position. Within 110 ps, significant diffusion of Al atoms from the core, through the ∼1 nm oxide shell, into the external Ni shell can be clearly observed. This process underscores the high mobility of Al at elevated temperatures and the permeability of the oxide shell under these conditions.

The diffusion process is accompanied by a marked decrease in the potential energy of the entire system, as illustrated by the blue curve in Figure 7d. The total potential energy drops by approximately 6000 kcal/mol, indicating an exothermic process. Concurrently, the number of Al−Ni bonds increases substantially, with ∼1400 new Al−Ni bonds forming, as shown by the green curve in Figure 7d. This bond formation highlights the strong interaction and chemical affinity between diffusing Al atoms and the surrounding Ni shell. The oxide shell is not affected significantly since the number of Al−O bonds is almost unchanged during the simulation. The MD simulation shows that Al atoms predominantly diffuse through the oxide shell, while both the oxide shell and the Ni layer remain stationary, which is consistent with TEM observations.

4. CONCLUSION

This study presents a scalable, one-pot synthesis method for Al@Ni nanoparticles, demonstrating the significantly reduced ignition temperature in nanothermite mixtures with CuO and enhanced burning rates in the HTPB/AP-based propellant. The modulation of the ignition temperature is achieved through the kinetic control of Ni condensation on Al particles. DSC, in situ TEM, and reactive MD simulations, reveal that the decreased ignition temperature of Al@Ni arises from two primary mechanisms: the exothermic Al−Ni alloying reaction and the inhibition of Al nanoparticle sintering. The findings indicate that the diffusion of Al through the oxide shell into Ni plays a crucial role in enabling exothermic Al−Ni alloying reactions in a relatively low temperature range. This comprehensive understanding of Al@Ni combustion mechanisms offers a pathway to optimizing energetic materials with lower ignition temperatures and superior performance.

■ ASSOCIATED CONTENT

Supporting Information

The Supporting Information is available free of charge at https://pubs.acs.org/doi/10.1021/acsaenm.5c00272.

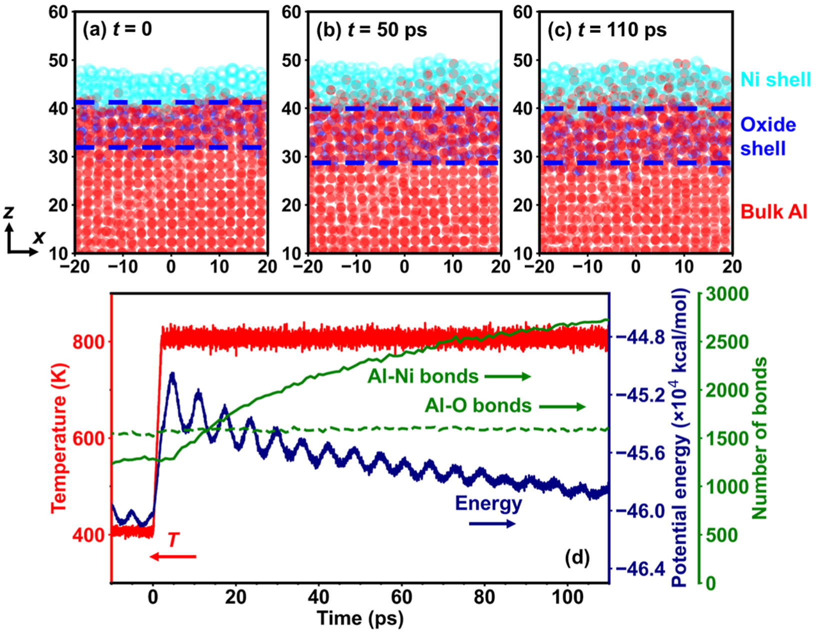

Figure 7. (a−c) Snapshots of stacked Al, Al_2O_3, and Ni layers (sliced view, 1 nm thickness) at $t = 0$, 50, and 110 ps, respectively; x,z units: Å. Al, O, and Ni atoms are represented by red, blue, and cyan symbols, respectively. (d) Time-evolution of temperature (red), potential energy (navy blue), and number of Al−Ni bonds (green). $t = 0$ is defined as where the entire system starts to increase the temperature from 400 to 800 K.

SEM images and particle size distributions of Al nanoparticles before/after Ni coating; raw TGA/DSC profiles of Al@Ni, PM Al−Ni Al_2O_3@Ni and control Al; Al−Ni phase diagram and its interpretation; XRD profile of the postproduct of Al@Ni after TG experiment; In situ TEM observations of Al@Ni and Al_2O_3@Ni; formulation of synthesized Al@Ni, Al_2O_3@Ni, and control Al; Average ignition delay times and ignition temperatures of Al@Ni and control Al; and thermochemical processes observed in TG-DSC experiments of Al@Ni, PM Al−Ni, and control Al (PDF)

AUTHOR INFORMATION

Corresponding Author

Michael R. Zachariah − *Departments of Chemical Engineering and Materials Science, University of California, Riverside, California 92521, United States;* orcid.org/0000-0002-4115-3324; Email: mrz@engr.ucr.edu

Authors

Yuxin Zhou − *Departments of Chemical Engineering and Materials Science, University of California, Riverside, California 92521, United States;* orcid.org/0009-0005-1397-3834

Lei Yang − *Departments of Chemical Engineering and Materials Science, University of California, Riverside, California 92521, United States;* orcid.org/0000-0002-1094-8642

Ashvin Kumar Vasudevan − *Departments of Chemical Engineering and Materials Science, University of California, Riverside, California 92521, United States*

Matthew Dickson − *Departments of Chemical Engineering and Materials Science, University of California, Riverside, California 92521, United States*

Mahbub Chowdhury − *Departments of Chemical Engineering and Materials Science, University of California, Riverside, California 92521, United States*

Keren Shi − *Departments of Chemical Engineering and Materials Science, University of California, Riverside, California 92521, United States*

Complete contact information is available at:
https://pubs.acs.org/10.1021/acsaenm.5c00272

Author Contributions

[†]Yuxin Zhou and Lei Yang are equal contributors to this work and designated as co-first authors.

Notes

The authors declare no competing financial interest.

ACKNOWLEDGMENTS

This work was supported by the DTRA MSEE-URA and the ONR.

REFERENCES

(1) Sundaram, D.; Yang, V.; Yetter, R. A. Metal-Based Nanoenergetic Materials: Synthesis, Properties, and Applications. *Prog. Energy Combust. Sci.* **2017**, *61*, 293−365.

(2) Sundaram, D. S.; Puri, P.; Yang, V. A General Theory of Ignition and Combustion of Nano- and Micron-Sized Aluminum Particles. *Combust. Flame* **2016**, *169*, 94−109.

(3) Chowdhury, S.; Sullivan, K.; Piekiel, N.; Zhou, L.; Zachariah, M. R. Diffusive vs Explosive Reaction at the Nanoscale. *J. Phys. Chem. C* **2010**, *114* (20), 9191−9195.

(4) Sullivan, K. T.; Piekiel, N. W.; Wu, C.; Chowdhury, S.; Kelly, S. T.; Hufnagel, T. C.; Fezzaa, K.; Zachariah, M. R. Reactive Sintering: An Important Component in the Combustion of Nanocomposite Thermites. *Combust. Flame* **2012**, *159* (1), 2−15.

(5) Egan, G. C.; Sullivan, K. T.; LaGrange, T.; Reed, B. W.; Zachariah, M. R. In Situ Imaging of Ultra-Fast Loss of Nanostructure in Nanoparticle Aggregates. *J. Appl. Phys.* **2014**, *115* (8), 084903.

(6) Chakraborty, P.; Zachariah, M. R. Do Nanoenergetic Particles Remain Nano-Sized during Combustion? *Combust. Flame* **2014**, *161* (5), 1408−1416.

(7) Zhou, Y.; Shi, K.; Chowdhury, M.; Hagen, E.; Wang, Y.; Zachariah, M. R. Direct Microscopic Imaging of Exploding Aluminum/Nitrocellulose Mesoparticles to Reveal the Enhanced Combustion Mechanism. *Fuel* **2025**, *387*, 134348.

(8) Zhou, Y.; Zachariah, M. R. Molecular Dynamics Study on the Capture of Aluminum Particles by Carbon Fibers during the Propagation of Aluminum-Based Energetics. *Energy Fuels* **2024**, *38* (10), 8992−9000.

(9) Dreizin, E. L. Metal-Based Reactive Nanomaterials. *Prog. Energy Combust. Sci.* **2009**, *35* (2), 141−167.

(10) Guan, F.; Ren, H.; Zhao, W.; Wu, X.; Jiao, Q. Novel Aluminum-Based Fuel: Facile Preparation to Improve Thermal Reactions. *Defence Technology* **2022**, *18* (10), 1852−1862.

(11) Jiang, Y.; Wang, Y.; Baek, J.; Wang, H.; Gottfried, J. L.; Wu, C.-C.; Shi, X.; Zachariah, M. R.; Zheng, X. Ignition and Combustion of Perfluoroalkyl-Functionalized Aluminum Nanoparticles and Nanothermite. *Combust. Flame* **2022**, *242*, 112170.

(12) Ali, R.; Ali, F.; Zahoor, A.; Shahid, R. N.; Tariq, N. U. H.; Ali, G.; Ullah, S.; Shah, A.; Awais, H. B. Preparation and Oxidation of Aluminum Powders with Surface Alumina Replaced by Iron Coating. *J. Energ. Mater.* **2022**, *40* (3), 243−257.

(13) Wang, C.; Zou, X.; Yin, S.; Wang, J.; Li, H.; Liu, Y.; Wang, N.; Shi, B. Improvement of Ignition and Combustion Performance of Micro-Aluminum Particles by Double-Shell Nickel-Phosphorus Alloy Coating. *Chem. Eng. J.* **2022**, *433*, 133585.

(14) Zhang, J.; Zhao, F.; Li, H.; Yuan, Z.; Zhang, M.; Yang, Y.; Pei, Q.; Wang, Y.; Chen, X.; Qin, Z. Improving Ignition and Combustion Performance of Al@Ni in CMDB Propellants: Effect of Nickel Coating. *Chem. Eng. J.* **2023**, *456*, 141010.

(15) Foley, T. J.; Johnson, C. E.; Higa, K. T. Inhibition of Oxide Formation on Aluminum Nanoparticles by Transition Metal Coating. *Chem. Mater.* **2005**, *17* (16), 4086−4091.

(16) Xiao, F.; Chen, C.; Zhang, Y.; Wen, X.; Zhang, J.; Liu, W.; Yang, Y. In Situ Preparation of Aluminum-Copper Pentafluorobenzoate Energy Microspheres: Enhancing Aluminum Combustion Properties in Composite Propellants. *Combust. Flame* **2024**, *267*, 113605.

(17) Hahma, A.; Gany, A.; Palovuori, K. Combustion of Activated Aluminum. *Combust. Flame* **2006**, *145* (3), 464−480.

(18) Li, Y.; Chen, Y.; Cui, W.; Tang, W.; Wang, B.; Han, Z. Preparation of Al/Ni Nano-Composite Particles via Replacement Reaction and Their Characterization. *ChemistrySelect* **2020**, *5* (43), 13673−13677.

(19) Andrzejak, T. A.; Shafirovich, E.; Varma, A. Ignition Mechanism of Nickel-Coated Aluminum Particles. *Combust. Flame* **2007**, *150* (1), 60−70.

(20) Kim, K. T.; Kim, D. W.; Kim, S. H.; Kim, C. K.; Choi, Y. J. Synthesis and Improved Explosion Behaviors of Aluminum Powders Coated with Nano-Sized Nickel Film. *Appl. Surf. Sci.* **2017**, *415*, 104−108.

(21) Kim, S.; Lim, J.; Lee, S.; Jeong, J.; Yoon, W. Study on the Ignition Mechanism of Ni-Coated Aluminum Particles in Air. *Combust. Flame* **2018**, *198*, 24−39.

(22) Kim, G.; Na, C. W.; Myung, Y. Facile One-Pot Synthesis of Nickel Nanoparticles by Hydrothermal Method. *Materials* **2023**, *16* (1), 76.

(23) Lai, Q.; Rawal, A.; Quadir, M. Z.; Cazorla, C.; Demirci, U. B.; Aguey-Zinsou, K.-F. Nanosizing Ammonia Borane with Nickel: A Path toward the Direct Hydrogen Release and Uptake of B-N-H Systems. *Adv. Sustainable Syst.* **2018**, *2* (4), 1700122.

(24) Yang, L.; Zhou, Y.; Chowdhury, M.; Qin, Y.; Dickson, M. M.; Zachariah, M. R. Synergistic Transition Multi-Metal Coatings Drive Sub-Melting-Point Reaction of Aluminum. *Chem. Eng. J.* **2025**, *519*, 164794.

(25) Zhou, L.; Piekiel, N.; Chowdhury, S.; Zachariah, M. R. T-Jump/Time-of-Flight Mass Spectrometry for Time-Resolved Analysis of Energetic Materials. *Rapid Commun. Mass Spectrom.* **2009**, *23* (1), 194−202.

(26) Zhou, L.; Piekiel, N.; Chowdhury, S.; Zachariah, M. R. Time-Resolved Mass Spectrometry of the Exothermic Reaction between Nanoaluminum and Metal Oxides: The Role of Oxygen Release. *J. Phys. Chem. C* **2010**, *114* (33), 14269−14275.

(27) Thompson, A. P.; Aktulga, H. M.; Berger, R.; Bolintineanu, D. S.; Brown, W. M.; Crozier, P. S.; in 't Veld, P. J.; Kohlmeyer, A.; Moore, S. G.; Nguyen, T. D.; Shan, R.; Stevens, M. J.; Tranchida, J.; Trott, C.; Plimpton, S. J. LAMMPS - a Flexible Simulation Tool for Particle-Based Materials Modeling at the Atomic, Meso, and Continuum Scales. *Comput. Phys. Commun.* **2022**, *271*, 108171.

(28) Zou, C.; Shin, Y. K.; van Duin, A. C. T.; Fang, H.; Liu, Z.-K. Molecular Dynamics Simulations of the Effects of Vacancies on Nickel Self-Diffusion, Oxygen Diffusion and Oxidation Initiation in Nickel, Using the ReaxFF Reactive Force Field. *Acta Mater.* **2015**, *83*, 102−112.

(29) Shin, Y. K.; Kwak, H.; Zou, C.; Vasenkov, A. V.; van Duin, A. C. T. Development and Validation of a ReaxFF Reactive Force Field for Fe/Al/Ni Alloys: Molecular Dynamics Study of Elastic Constants, Diffusion, and Segregation. *J. Phys. Chem. A* **2012**, *116* (49), 12163−12174.

(30) Zheng, Y.; Hong, S.; Psofogiannakis, G.; Rayner, G. B., Jr.; Datta, S.; van Duin, A. C. T.; Engel-Herbert, R. Modeling and in Situ Probing of Surface Reactions in Atomic Layer Deposition. *ACS Appl. Mater. Interfaces* **2017**, *9* (18), 15848−15856.

(31) Evans, D. J.; Holian, B. L. The Nose−Hoover Thermostat. *J. Chem. Phys.* **1985**, *83* (8), 4069−4074.

(32) Lee, H.; Kim, J. H.; Kang, S.; Deshmukh, P. R.; Sohn, Y.; Hyun, H. S.; Shin, W. G. Ignition of Nickel Coated Aluminum Agglomerates Using Shock Tube. *Combust. Flame* **2020**, *221*, 160−169.

(33) Bao, S.; Li, T.; Guo, C.; Zhao, Y.; Zhang, H.; Wu, R.; Shi, H. One-Pot Preparation of HTPB/nNi and Its Catalyst for AP. *Nanomaterials* **2022**, *12* (15), 2669.

(34) Yu, H.; Yu, X.; Gao, H.; DeLuca, L. T.; Zhang, W.; Shen, R. Combustion Characteristics of HTPB-Based Hybrid Rocket Fuels: Using Nickel Oxide as the Polymer Matrix Pyrolysis Catalyst. *Aerospace* **2023**, *10* (9), 800.

(35) Wang, Y.; Zhu, J.; Yang, X.; Lu, L.; Wang, X. Preparation of NiO Nanoparticles and Their Catalytic Activity in the Thermal Decomposition of Ammonium Perchlorate. *Thermochim. Acta* **2005**, *437* (1), 106−109.

(36) Cojocaru, M.; Tudose, F. The Obtaining of the Intermetallic Compounds of Ni-Al System by Self-Propagating High Temperature Synthesis and Thermal Explosion. *Adv. Mater. Res.* **2015**, *1114*, 135−142.

(37) Cheng, J. L.; Hng, H. H.; Ng, H. Y.; Soon, P. C.; Lee, Y. W. Deposition of Nickel Nanoparticles onto Aluminum Powders Using a Modified Polyol Process. *Mater. Res. Bull.* **2009**, *44* (1), 95−99.

(38) Philpot, K. A.; Munir, Z. A.; Holt, J. B. An Investigation of the Synthesis of Nickel Aluminides through Gasless Combustion. *J. Mater. Sci.* **1987**, *22* (1), 159−169.

(39) Zhu, P.; Li, J. C. M.; Liu, C. T. Combustion Reaction in Multilayered Nickel and Aluminum Foils. *Mater. Sci. Eng., A* **1997**, *239−240*, 532−539.

(40) Chrifi-Alaoui, F. Z.; Nassik, M.; Mahdouk, K.; Gachon, J. C. Enthalpies of Formation of the Al−Ni Intermetallic Compounds. *J. Alloys Compd.* **2004**, *364* (1), 121−126.

(41) Sehested, J.; Gelten, J. A. P.; Remediakis, I. N.; Bengaard, H.; Nørskov, J. K. Sintering of Nickel Steam-Reforming Catalysts: Effects of Temperature and Steam and Hydrogen Pressures. *J. Catal.* **2004**, *223* (2), 432−443.

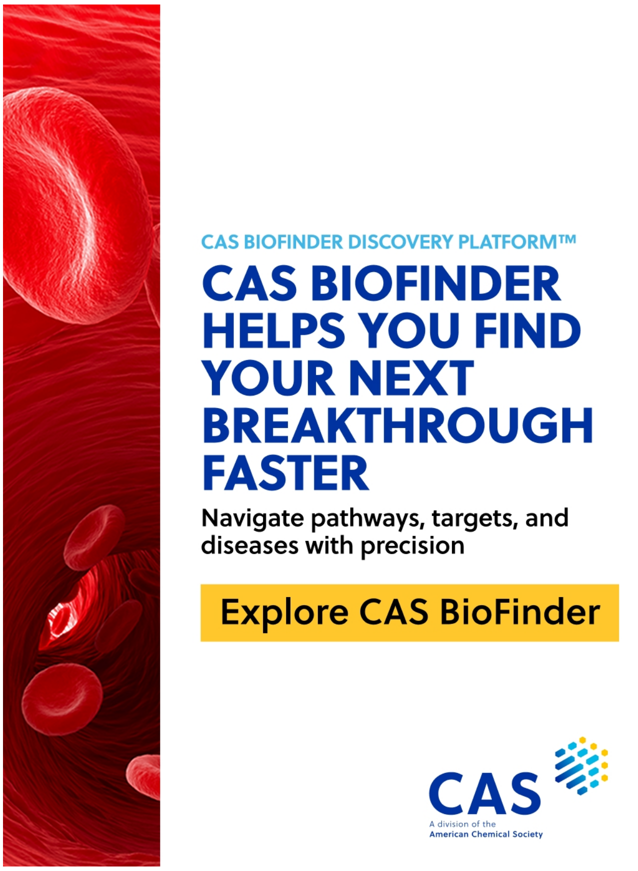

CAS BIOFINDER DISCOVERY PLATFORM™

CAS BIOFINDER HELPS YOU FIND YOUR NEXT BREAKTHROUGH FASTER

Navigate pathways, targets, and diseases with precision

Explore CAS BioFinder

CAS
A division of the American Chemical Society